Acta Materialia 239 (2022) 118261

Contents lists available at ScienceDirect

Acta Materialia

journal homepage: www.elsevier.com/locate/actamat

Phase transformations and microstructure evolution during combustion of iron powder

Laurine Choisez[a,*], Niek E. van Rooij[b], Conrad J.M. Hessels[b], Alisson K. da Silva[a], Isnaldi R. Souza Filho[a], Yan Ma[a], Philip de Goey[b], Hauke Springer[a,c], Dierk Raabe[a]

[a] Max-Planck-Institut für Eisenforschung, Max-Planck-Str. 1, 40237 Düsseldorf, Germany
[b] Department of Mechanical Engineering, Eindhoven University of Technology, PO Box 513, 5600MB Eindhoven, the Netherlands
[c] Institut für Bildsame Formgebung, RWTH Aachen University, Intzestr. 10, 52072 Aachen, Germany

ARTICLE INFO

Article history:
Received 20 March 2022
Revised 24 June 2022
Accepted 10 August 2022
Available online 10 August 2022

Keywords:
Metal fuel
Sustainable energy carrier
Iron powder
Combustion
Solidification microstructure

ABSTRACT

To successfully transition from fossil-fuel to sustainable carbon-free energy carriers, a safe, stable and high-density energy storage technology is required. The combustion of iron powders seems very promising in this regard. Yet, little is known about their in-process morphological and microstructural evolution, which are critical features for the circularity of the concept, especially the subsequent reduction of the combusted oxide powders back to iron. Here, we investigated two iron powder combustion pathways, one in air and one with the assistance of a propane pilot flame. Both processes resulted in spherical hollow particles composed of a complex microstructure of wüstite, magnetite and/or hematite. Partial evaporation is indicated by the observation of nanoparticles on the micro-sized combustion products. The associated gas production inside the liquid droplet could be the origin of the internal porosity and micro-explosion events. Cracking at the end of the combustion process results in mostly open porosity, which is favorable for the subsequent reduction process. With this study, we aim to open the perspective of iron metal fuel from macroscopic combustion analysis towards a better understanding of the underlying microscopic thermodynamic, kinetic, microstructural and thermomechanical mechanisms.

1. Introduction

One of the most pressing problems to solve in our changing energy system is to deploy efficient storage and transport vectors. Batteries are not suitable for large-scale and long-term storage due to their comparatively high manufacturing costs, challenging material requirements and insufficient sustainability and recyclability. Hydrogen has a very high mass-specific energy density (33 kWh/kg), but a low volumetric energy density of 3 Wh/L at room temperature and atmospheric pressure [1]. Hydrogen thus needs to be stored at high pressure (250–350 bar) or at very low temperatures (20–150 K), to obtain sufficiently high volumetric energy densities [1]. Liquifying hydrogen requires up to 40% of its energy content [2] and hydrogen storage can lead to embrittlement of the containers. A low-cost and energy-dense alternative comes in the form of metal powder and the corresponding metal energy carrier concept [2–7]. Energy production is obtained through the heat of oxidation of these metallic powders, bringing a very large energy density compared with other energy storing systems (Fig. 1). Renewable energy can be used to reduce consumed metal oxide fuels back to metal, which can then be again combusted (= oxidized) whenever and wherever energy is needed.

Most research on this metal energy carrier concept has focused on the combustion of iron powder, where ignited single particles [8–11], small burners [12–16], and stagnant aerosols [17,18] have been studied experimentally, and some initial numerical models [19–21] have also been developed. Various metal particle combustion modes have been proposed in the literature [4,22]. When the flame temperature is above the boiling point of the metal, a micro-diffusion flame is formed with oxidation occurring at the gaseous state, which is referred to as homogeneous combustion mode. When the flame temperature is below the boiling point of the metal, the oxidation occurs at the surface of the metal particle, and it is referred to as heterogeneous combustion mode. In the latter mode, depending on the relative metal oxide vapor pressure at the flame temperature, gaseous metal oxide forms and condenses away from the particle, or oxide combustion products form directly on the surface of the metal particle [4]. Iron is particularly suited as a renewable fuel as its oxides mainly form at the surface of the particle, forming combustion products of similar size as the initial iron powder. In contrast, other metals have the tendency to form gaseous metal oxides which solidify as nanoparticles, a sce-

* Corresponding author.
E-mail address: l.choisez@mpie.de (L. Choisez).

https://doi.org/10.1016/j.actamat.2022.118261
1359-6454/

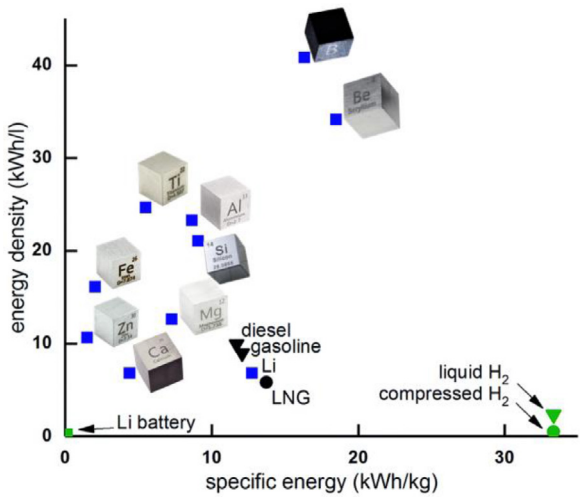

Fig. 1. Energy density and specific energy of various metals compared with batteries, hydrogen and fossil fuels. Adapted from Bergthorson et al. [4,49].

nario that is undesired from a circularity perspective (difficult to collect and reduce), arising also health and safety concerns [4,22]. Only small fractions of nanoparticles during the combustion of iron powders have been reported, mostly occurring in excess-oxygen conditions [6,8,9,11–14,16,17].

The oxidation of iron in the solid-state is a well-known and deeply investigated topic. The underlying mechanism is considered as follows [23]: (1) Diffusion of the oxygen molecules from the surrounding gas to the surface of the oxide layer; (2) Incorporation of the oxygen anions into the oxide layer; (3) Absorption of the iron cations at the oxide/metal boundary; (4) Diffusion of the ions and electrons through the oxide layers; (5) Reaction at the interfaces. At relatively high temperature (700–1250 °C), the growth rate of the oxide scales follows a parabolic law, showing that the limiting step of the reaction is the ion diffusion through the oxide layers [24]. Because of their lower size and larger vacancy density, the mobility of iron cations is larger that of oxygen anions during the oxidation process [23,25], thus the rate-limiting step of solid-state oxidation of pure iron is the outward diffusion of iron cations [26]. However, the oxidation mechanism of iron in the liquid state is much less understood. Hirano et al. [27] proposed a mechanism similar to the oxidation in the solid-state for the oxidation of a metal droplet at the tip of an iron cylinder and suggested the following steps: (1) diffusion of the oxygen molecules from the surrounding gas to the surface of the liquid; (2) oxygen adsorption on the molten oxide surface, which includes the physical adsorption of the oxygen molecule, the chemical adsorption of the dissociated oxygen atoms, and the incorporation of the oxygen atoms inside the oxide layer; (3) ionic diffusion through the oxide layer; and (4) reaction at the oxide/metal boundary. According to Hirano et al. [27,28], the rate-limiting step of the reaction is the adsorption of oxygen at the surface of the liquid droplet. Yet, the reaction at the interface of molten iron and liquid iron oxide was also considered to be the rate-limiting step of the oxidation of a liquid droplet at the tip of an iron rod because of the coexistence of both liquid iron and liquid iron oxide phase [29]. This oxidation mechanism was later also considered for the combustion of small individual iron particles in air by several authors [8,13,30]. Depending on the oxygen diffusion rate from the surrounding atmosphere to the surface of the droplet relative to the adsorption of oxygen at the particle surface, the combustion process is said to follow either a kinetic-controlled regime, i.e. limited by the reaction process and in particular by the adsorption step, or a diffusion-controlled regime, i.e. limited by oxygen diffusion to the surface of the particle [22]. Because of the low activation energy and high flame temperature of metal combustion, the combustion process is generally limited by the oxygen diffusion [12]. The diffusion-controlled regime is particularly favored for large particle sizes [22], and has been reported by several authors for an iron particle size over 5 µm [8,12,13]. A transitional regime corresponding neither to the kinetic-controlled nor to the diffusion-controlled regime was measured by Tang et al. [22] for an iron particle size of 3 µm in 21 at.% oxygen. Ning et al. [8] also identified a transitional regime as a second part of the combustion mechanism, starting in a diffusion-controlled regime when the particle temperature is increasing, then becoming more independent from the oxygen concentration for the later part of the combustion process. They proposed that the end of the combustion process could be limited by the internal diffusion of oxygen inside the particle instead of the external diffusion of oxygen to the surface of the particle [8]. While several models have been proposed [4,8,22], the nature and course of the different mechanisms involved in the combustion of iron powders are not yet completely understood.

Moreover, little is known about the microstructural, chemical and morphological evolution of the iron powders during the combustion process. The combustion products are reported to be generally spherical, hollow and containing many pores and cracks [6,9,11,12]. However, no detailed studies have been conducted yet on the quantity and distribution of the porosity and cracks formed during the combustion process. Of high interest are also the specific thermodynamic states and types of oxides produced. Because of the large heating and cooling rate involved (around 40,000–50,000 $K \cdot s^{-1}$ [9]), the conditions deviate from the thermodynamic predicted conditions documented in the equilibrium phase diagram [12]. Based on the temperature evolution of single burning iron particles experiments, Ning et al. [9] predicted a phase transformation to either magnetite or hematite at the end of the combustion process. Poletaev et al. [13] also reported combustion products mainly composed of magnetite. However, the phase transformation paths involved in the combustion process are mostly unknown from previous experiments.

The final microstructure and morphology will greatly impact the reduction process of combusted powders, necessary to ensure circularity of the technology (and thus its sustainability and economic viability), by a direct reduction process using hydrogen [31–35]. Hence, the analysis of the combusted particles is critical for understanding the fundamental mechanisms involved in the combustion process, involving the different phase transformations, crack and porosity formation, and optimizing the subsequent reduction process. These scientific insights can also serve as a knowledge platform to custom design iron-based alloys for a more efficient metal energy carrier and possibly even aid in better understanding some of the microscale mechanisms in sustainable steel production with hydrogen.

2. Materials and methods

Two batches of iron powder, referred hereafter to as InitAir and InitPro in this manuscript, were provided by Pometon S.p.A.. The material was produced via water atomization from scrap metal and are only differentiated by a slightly different impurity content (given below in Table 1). The powder was subsequently combusted in a pilot scale industrial burner. The first batch, InitAir, was combusted in pre-heated air using only propane to start the ignition in the beginning of the process and punctually to prevent the iron powder flame from extinguishing if required. The combusted powder produced by this combustion process is hereafter referred to as OxAir. The second batch, InitPro, was combusted with a continuous addition of propane, bringing one third of the total heat during the combustion process. The combusted powder is called OxPro here-

Table 1
Composition in weight percent of the initial powder and the combusted powder measured by ICP-OES, reduction fusion and the combustion method (InitAir and OxAir for the combustion in air, and InitPro and OxPro for the combustion in air and propane). n.m. stands for not measured.

[wt.%]	O	C	S	Ni	Cu	Mn	Mo	Cr	P	Si	Fe
InitAir	0.57	0.019	0.010	0.095	0.088	0.063	0.043	0.027	0.007	0.003	Bal.
OxAir	21.8	0.006	0.003	0.154	0.088	0.043	0.023	0.020	0.004	0.006	Bal.
InitPro	n.m.	0.027	0.009	0.035	0.036	0.045	0.054	0.021	0.004	0.004	Bal.
OxPro	22.4	0.005	0.001	0.037	0.032	0.035	0.034	0.015	<0.002	<0.002	Bal.

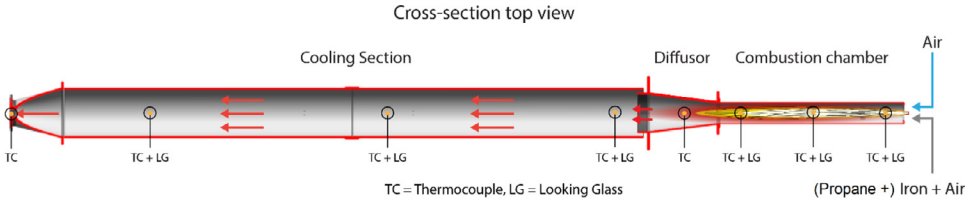

Fig. 2. Schematic of the burner. A center jet of iron, air and propane is surrounded by a co-flow of preheated air. After the cooling section a cyclone is placed to separate the powder from the gas.

after. A schematic of the burner used is presented in Fig. 2. The iron powder was injected together with some air. Additional preheated air was provided by a co-flow to reach an overall air fuel (iron) equivalence ratio (λ) between 3 and 5. The propane was provided using a separate injector, thus creating a non-premixed pilot flame. Before each experiment, propane was used to heat up the system. Subsequently, iron was slowly introduced and the propane flow was simultaneously decreased to the desired operating conditions. All flows were set by control valves in combination with flow meters. After leaving the combustion chamber, the powder was cooled in a cooling section, sorted in a cyclone and finally recovered. All particles analyzed in this paper were collected from the exit of the cyclone. The average temperature emitted by the burning particles was measured in different parts of the combustor: an Ocean Optics USB2000 UV–VIS spectrometer was used to analyze the radiation in the range of 200–900 nm emitted in the combustion chamber for temperatures over 1200 °C via the looking glasses, and thermocouples were used in the cooling chamber for temperatures below 1300 °C (see Fig. 2). OxPro powder was quasi instantaneously ignited after injection due to the propane pilot flame, reaching a maximum temperature of 1850–2200 °C, while OxAir powder was more gradually ignited, with a maximum temperature of 1900–2100 °C reached after about 1 s. The full estimated profile of the mean temperature of the powders as a function of the residence time in the combustor is given in Supplementary Figure S1.

The size and shape distribution of the powders were derived from Dynamic Image Analysis conducted using a 3P instruments Bettersizer S3 Plus using isopropanol as a dispersant. Over 5000 individual particles where imaged for each powder. The projected area diameter, d_a, defined as the diameter of a circle with equivalent projected area as the measured particle, is presented. Circularity is defined as $\frac{\pi d_a}{P}$, with P the measured perimeter of the particle and d_a the diameter of a circle having the same cross-sectional area as the particle. All distributions are expressed by a volume-based statistic. The microstructure and morphology of the powders were characterized by scanning electron microscopy (SEM) and electron backscatter diffraction (EBSD). The powders were either dispersed on a copper tape and coated with 25 nm of carbon to observe their surface morphology, or embedded and metallographically prepared to observe their cross-sections. EBSD maps were acquired using a JEOL-6500F field-emission gun microscope. Energy-dispersive X-ray spectroscopy (EDS) analyzes were also conducted using a Zeiss Sigma SEM with an accelerating voltage of 15 kV. Image analysis was applied using Fiji ImageJ software [36] to estimate the porosity level from SEM micrographs of the cross-section of the powders. Close porosity is defined as the ratio between the area of the porosity encapsulated in the particle, i.e. not linked to the external surface, and the area of the filled particle, i.e. the addition of the section of the particle and of the encapsulated voids. An example of the binary images resulting from the image analysis is presented in Supplementary Figure S1. An automatic approach was used on several SEM images, analyzing more than 1000 particles for each powder. A minimum of 9 pixels square (about 0.45 μm^2) was set to detect the porosity. More details can be found in the Supplementary Materials. The average composition of the powders was characterized by inductively coupled plasma optical emission spectrometry (ICP-OES) and averaged on two measurements. The oxygen content was determined via reduction fusion under a helium atmosphere and subsequent infrared absorption spectroscopy. Carbon and sulfur were analyzed via combustion followed by infrared absorption spectroscopy. About 0.5 g of powder was used for each measurement of the chemical composition. Phase identification and quantification were obtained by X-ray diffraction (XRD) measurements, using a diffractometer D8 Advance A25-X1, equipped with a cobalt target, operated at 35 kV, 40 mA. The powders were previously sieved under 90 µm, then dispersed on a sample holder of 3 mm in diameter. Four sampling of 0.5 g of the combusted powders were applied to obtain a better statistical representation of the phase distribution. The diffraction data were processed using the software Brucker Topas v. 5.0. with the Rietveld refinement. Pycnometer measurements were applied using AccuPyc II 1340 V3.00 under argon at room temperature. The solid phase apparent density of the powders was estimated by weighting the total mass of the powder, between 18 g and 26 g, which was divided by the total volume measured by pycnometer (including the closed porosity), averaged on 5 gas filling cycles. It must be noted than important statistical effects can be expected from each measurement, as they were all applied on relatively small quantities compared with the total mass of combusted powder (about 500 kg).

Equilibrium adiabatic calculations were performed using the Thermocalc software [37] together with the TCS Metal Oxide Solutions Database (TCOX10) for the description of the condensed phases and the SSUB5 SGTE (Scientific Group Thermodata Europe) Substances Database for the description of the gas phase including metallic and oxide vapors. The equilibrium adiabatic temperature of the system was calculated assuming that an increasing amount of air (mechanical mixture of 21 at.% O_2 and 79 at.% N_2 at their stable element reference state, i.e., 25 °C and 1 atm) is added to

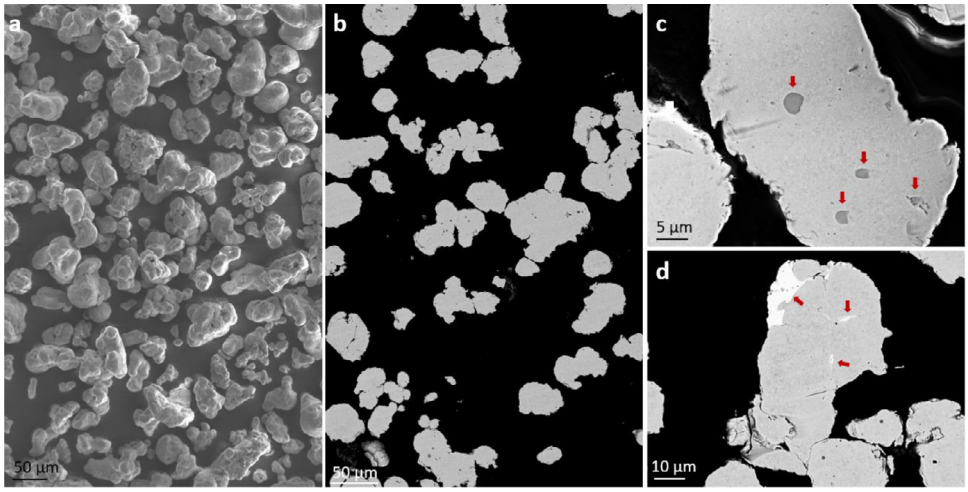

Fig. 3. SEM micrographs of the initial iron powder (a) Surface morphology; (b) cross section; (c) impurities present as oxide particles and (d) as a second phase as indicated by red arrows.

the open system containing 100 g of the initial composition of the powder. For a process taking place under adiabatic and isobaric conditions, the first law renders that the change of enthalpy of the system should be equal to zero (dH = 0), and the second law states that the entropy change of the system (dS) should be equal to the entropy production of the internal process ($d_{ip}S$). Equilibrium temperature and phase fractions are achieved when the entropy production reaches a maximum, i.e. when $d_{ip}S/d\xi = 0$ where ξ is the extent of the reaction [38]. Thermocalc, like most programs for the computation of equilibria, works by first minimizing the Gibbs energy at different temperatures and phase fractions to find the state in which the enthalpy of the system is conserved (dH = 0). Since only a homogeneous reaction can proceed to the same extent ξ in all parts of the system under adiabatic and isobaric conditions, those calculations should be regarded as a first approximation which works best at higher temperatures and assuming liquid and gaseous phases [38].

The two batches of initial powder are very similar to each other as they result from the same manufacturing process, presenting only a slight variation in impurities content, as given in Table 1. The oxygen content was only measured in the first batch (InitAir), but is expected to be similar to the oxygen content of the second batch (InitPro). The volume-based size distribution measured in the first batch is given in Supplementary Figure S3: Dv10-Dv50-Dv90 particle sizes (indicating the upper size limit containing 10%, 50% and 90% of the volume of the powders) are 27–49–85 µm. It should be noted that a part of the particles, biased to the larger particles, did not reach the cyclone, hence a decrease in the combusted particle size is expected. The initial powders present an irregular morphology, as illustrated by its surface morphology and its cross section in Figs. 3(a-b). The shape distribution is given in Supplementary Figure S3, showing a maximum circularity around 0.87. Figs. 3(c-d) highlight the presence of impurities, formed either as oxide particles (containing about 0.8 wt.% Cr and 2.3 wt.% Mn in addition to Fe and O in Fig. 3c, as estimated via EDS) or as a metallic phase (containing more than 90 wt.% Cu in Fig. 3d).

3. Results

3.1. Macroscopic chemical and physical properties

The combusted powders using air and/or propane present a relatively similar size distribution: Dv10-Dv50-Dv90 particle sizes are 19–34–61 µm for OxPro and 21–35–56 µm for OxAir. Both combusted particle distributions also exhibit high circularity with a maximum around 0.95, although OxPro particles presents a slightly higher circularity compared with OxAir (Supplementary Figure S3).

The average composition of the initial and combusted powder is given in Table 1. A significant decrease in carbon and sulfur content is measured during the combustion, while the amount of other impurities stays relatively constant through the combustion process. The slight increase in certain impurities in the combusted powders, such as Ni in OxAir powder, can come from a statistical effect, i.e. a larger number of particles containing a concentrated amount of impurities were present in the sampling for ICP-OES.

Fig. 4 gives the phase distribution measured in the initial powder based on four XRD measurements on each powder, after combustion using propane (OxPro) and under pre-heated air (OxAir). The proportion of ferrite in OxAir powder was also estimated by image analysis of SEM images as 10.75 area%. Traces of wüstite were detected in OxAir powder, in too small quantity for the quantitative analysis (less than 1%).

Pycnometer measurements were applied to estimate the solid phase apparent density, decreasing from 7.82 $g.cm^{-3}$ for the initial powder to 5.38 $g.cm^{-3}$ for the OxPro powder, and to 5.13 $g.cm^{-3}$for the OxAir powder. A decrease in the solid phase density was expected from the oxidation of the powder, with a theoretical density decreasing from 7.87 $g.cm^{-3}$ for ferrite to 5.20 $g.cm^{-3}$ for magnetite and 5.24 $g.cm^{-3}$ for hematite [39].

3.2. Microstructure of OxPro powder

Fig. 5 presents the morphology of powder combusted using propane (OxPro). The external surface is either constituted of an arrangement of parallel lines (Fig. 5a) or of coarser blocks (Fig. 5b). In both cases, small cracks are often present at the surface of the particles, either following the patterns on the external surface or cutting through it, as highlighted by the white arrows in Fig. 5a and 5b.

While most of the combusted powder consists of close spherical particles, some particles present a different morphology. Fig. 5(c) shows a particle with an opening resembling an internal explosion event. Fig. 5(d) exhibits another open particle, with the edges of the opening crack presenting a flat dendritic morphology. Finally, Fig. 5(e) presents a particle split in two parts, containing many smaller spherical particles inside. Fig. 5(f) presents a cross-section of a similar hollow particle, showing a “matryoshka-doll” structure with the presence of many smaller spherical particles inside the

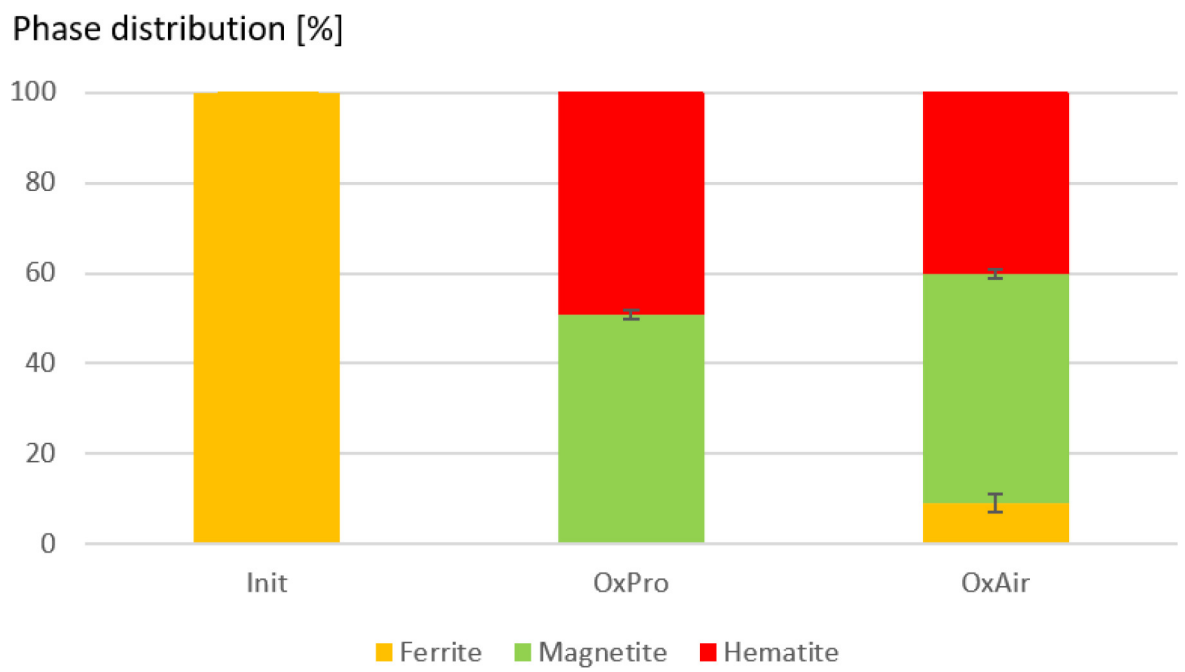

Fig. 4. Phase distribution in the initial and combusted powders measured by x-ray diffraction.

main particle, one of which even contains a smaller particle inside as highlighted by a white arrow.

The magnified micrograph shown in the inset of Fig. 5(d) highlights the presence of nanoparticles on the surface of the combusted particle. These nanoparticles present a size between 10 and 100 nm, but usually agglomerate in clusters of a few hundred nanometers. Such nanoparticles were found in the aftertreatment filters, as well as covering the walls of the combustor with a reddish color. However, these nanoparticles could not be separated from the micro-size particles for further analysis.

Fig. 6 presents cross-section views of these spherical combusted particles. Many particles are hollow, with a dendritic morphology occupying part of the hole as shown in Fig. 6(a). Moreover, many cracks are observed in the microstructure, following angular edges of the central cavity or starting from the external surface. Figs. 6(b) and 6(c) highlight the presence of two phases, identified in Fig. 7(b) as magnetite for the matrix and hematite highlighted here in white by the in-lens contrast. Hematite can form either as coarser grains at the external surface (Fig. 6(b)) or with a thin lenticular morphology (Fig. 6(c)). Fig. 6(d) reveals details of the link between the external surface of the powder (imaged using secondary electron contrast) and its internal microstructure (highlighted using back-scattered electron contrast). The linear pattern on the external surface presented in Fig. 5(a) correspond to the grain boundaries of the thin plates of hematite.

Fig. 7 presents an EBSD analysis of two combusted particles. The phase map in Fig. 7(b) shows that hematite plates grow from the external surface and from the inner void along the grain boundaries of the magnetite matrix. Fig. 7(c) presents the crystalline orientation of each grain. The black box in Fig. 7(c) and the associated pole figures in Fig. 7(d) show a crystallographic relationship between the grains of hematite and magnetite: (111) magnetite // (0001) hematite; [110] magnetite // [10$\bar{1}$0] hematite. Many cracks and inner porosity are present inside this particle, highlighted by white and black arrows respectively. An interesting observation can be made about the morphology and orientation of the hematite plates regarding these defects: the inner porosity (black arrows) effectively interrupts the hematite plates, presenting different morphologies and crystalline orientations at the opposite sides of the porosities. However, the lenticular plate morphologies and orientation are identical from either side of the cracks (white arrows), which do not interrupt the growth of hematite plates.

Fig. 7(e) presents a particle in which a third phase can be observed at the center of the particle, in a lighter contrast using back-scattered electron contrast. This third phase was identified as wüstite by EBSD in Fig. 7(f), and contains smaller magnetite grains inside. The shape of the wüstite grains is typical of interdendritic microstructure, with the dendrites constituting of magnetite in this case.

Most of the combusted powders are of high chemical purity compared with the initial Fe powder, i.e. only Fe and O are detected by EDS analysis. The impurities measured by ICP in the powders (Table 1) are concentrated in some specific particles in the form of gangue oxides. Fig. 8 presents a gangue-bearing particle composed of small gray domains that are embedded in a white matrix. Some of them display black submicron-size particles, as revealed in Fig. 8(b). The composition of the three-above mentioned constituents was estimated by EDS and is given in Fig. 8(b), although the exact composition cannot be obtained at this scale with this method because of the presence of light elements such as oxygen and of the fine microstructure with particles below 1 µm. Nevertheless, an increasing amount of aluminum can be observed from the white matrix to the darker particles.

3.3. Microstructure of OxAir powder

Two different morphologies are observed in OxAir powder as presented in Fig. 9(a). Their relative volume fraction was estimated by image analysis of the polished powders: 88% of the powder present a spherical shape similar to OxPro powder, while the remaining 12% (highlighted by black arrows in Fig. 9(a)) presents an irregular morphology similar to the initial powder. The same surface patterns as for OxPro powder are observed, covered with nanoparticles and sometimes containing cracks. The surface of the irregular-shape particles is constituted of a continuous porous deposit, with nanoparticles on top of the deposit. Open particles with a Matryoshka structure such as the ones highlighted in Fig. 5(e-f)

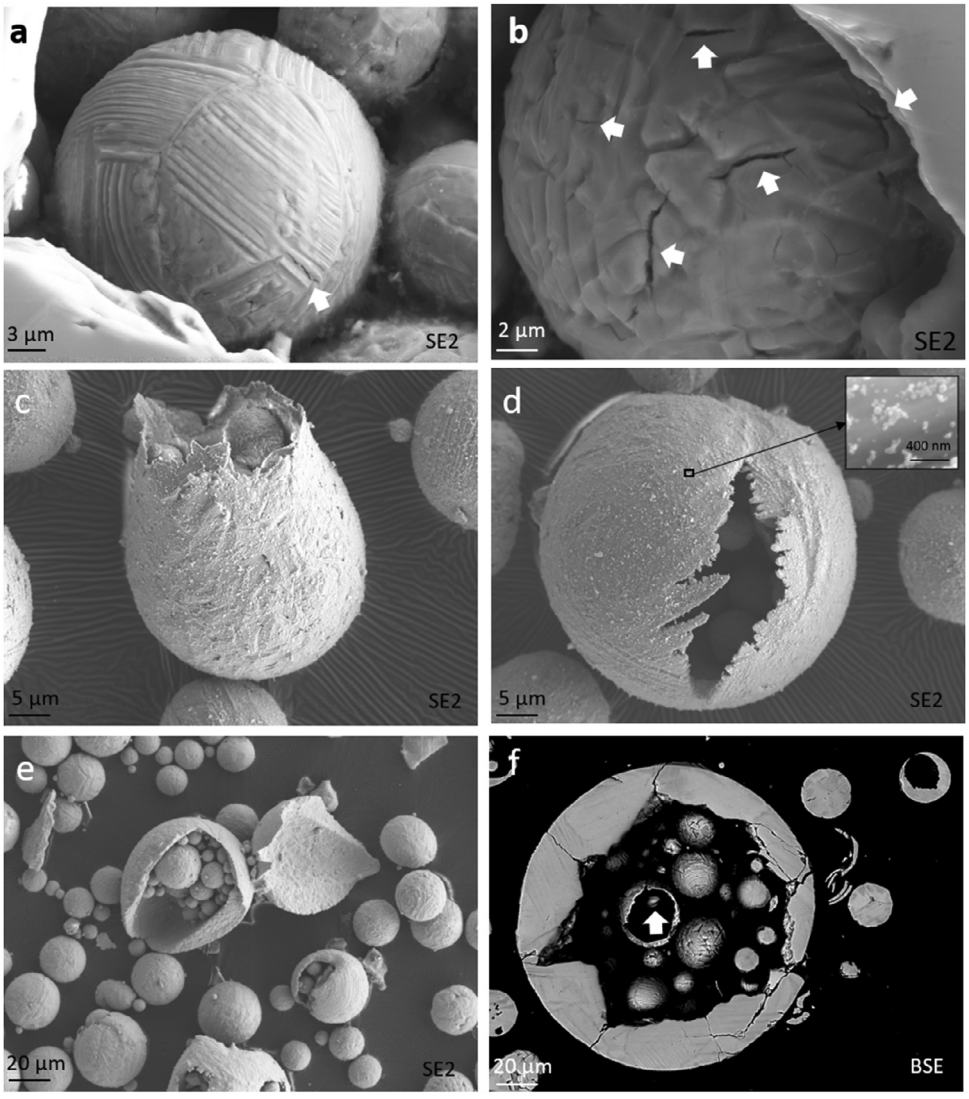

Fig. 5. SEM images of the morphology of OxPro powder. (a) and (b) External morphology of the powder, with the presence of cracks highlighted by white arrows. (c-e) Opened particles. (d) Magnified micrograph highlighting the presence of nanoparticles. (f) Cross-section of a hollow powder, showing the presence of smaller spherical particles inside. SE2 and BSE correspond to secondary electron and back-scattered electron contrast.

for OxPro particles are also observed, and Fig. 9(b) presents a cross-section of such morphology. The two morphologies identified in Fig. 9(a) are found inside the bigger cracked and hollow particle.

Figs. 9(c-e) present an EBSD analysis of the irregular-shape particle, constituted of ferrite grains with small oxide inclusions. The presence of 0.2 wt.% Si, 0.6 wt.% Cr and 1.8 wt.% Mn was detected by EDS in the small inclusions highlighted by a black arrow in Fig. 9(d), while only iron was detected in the matrix. The oxide shell is constituted of a dense wüstite layer close to the ferrite, surrounded by a magnetite layer. The spherical particles present a similar microstructure as the OxPro particles as highlighted in Fig. 9(f-h): a matrix of magnetite with hematite laths, with the same crystallographic relationship between the grains of hematite and magnetite: (111) magnetite // (0001) hematite; [110] magnetite // $[10\bar{1}0]$ hematite.

4. Discussion

Two types of morphologies were observed in the combusted powders: (1) spherical, generally hollow particles, similar to the reported morphology of the combustion products of ignited iron powders [6,9,11,12], and (2) irregular particles with a similar morphology as the initial iron particle. The latter presents a microstructure typical of solid-state iron oxidation [40]: an outer layer of magnetite and an internal layer of wüstite in-between the magnetite layer and the ferrite core, as well as magnetite precipitated in the wüstite (Fig. 9(d)). These particles were exposed to a lower temperature compared with the spherical particles, showing that they did not ignite. The presence of these irregular powder particles explains the smaller circularity values (Supplementary Figure S3) of OxAir particles compared with OxPro particles, which only contain spherical particles. Apart from the presence of non-ignited particles in OxAir powder, combusting the powder solely in air or with the help of propane results in a similar morphology/microstructure of the spherical ignited particles.

A peculiar feature observed in both powders is the formation of the “Matryoshka doll” arrangement, i.e. the presence of smaller particles inside bigger hollow ones, which can also contain smaller particles themselves (Figs. 5(e-f) and 9(a-b)). While only spherical iron oxide particles were found inside hollow shells in the OxPro powder, both iron oxide particles and irregular-shaped particles with a unoxidized iron core were observed inside hollow shells in

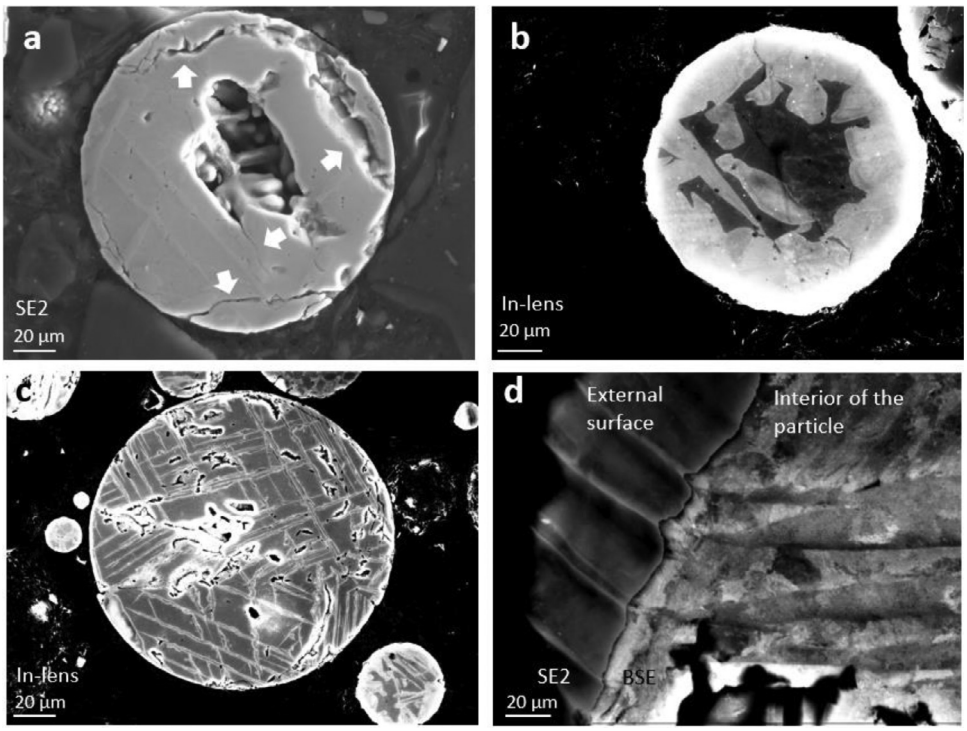

Fig. 6. SEM images of the cross section of OxPro powder, highlighting (a) numerous cracks and a dendritic morphology inside a central hole; (b) a second phase in the form of bulk grains near the external surface or (c) thin lenticular plates. (d) Superposition of two SEM images with different detectors to highlight the link between the lenticular plates and the surface linear morphology. BSE, SE2 and In-lens correspond to back-scattered electron, secondary electron and in-lens contrast, respectively.

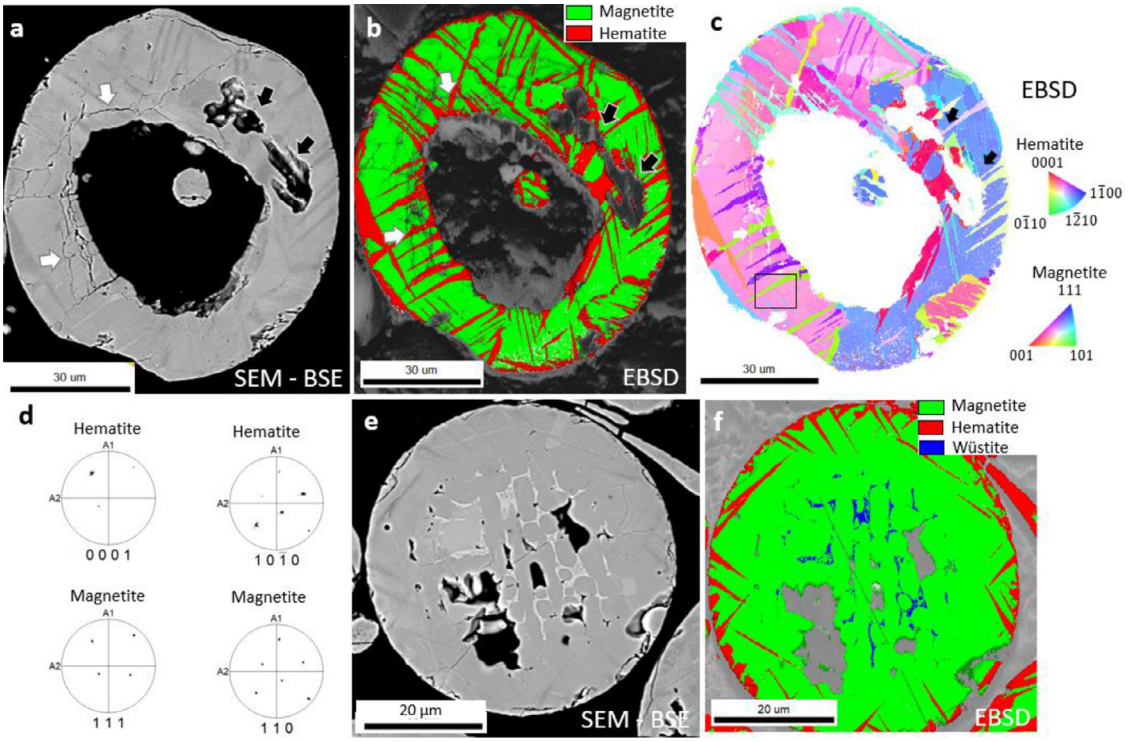

Fig. 7. Electron back-scattered diffraction (EBSD) analysis of OxPro particle. (a) SEM – back scattered electron (BSE) contrast, (b) phase map and image quality (c) inverse pole figure of a hollow particle. (d) Pole figures corresponding to the black box in (c). White and black arrows highlight cracks and larger porosity crossing hematite laths, respectively. (e) SEM-BSE image of a particle containing three different phases, as highlighted by the corresponding EBSD phase map in (f).

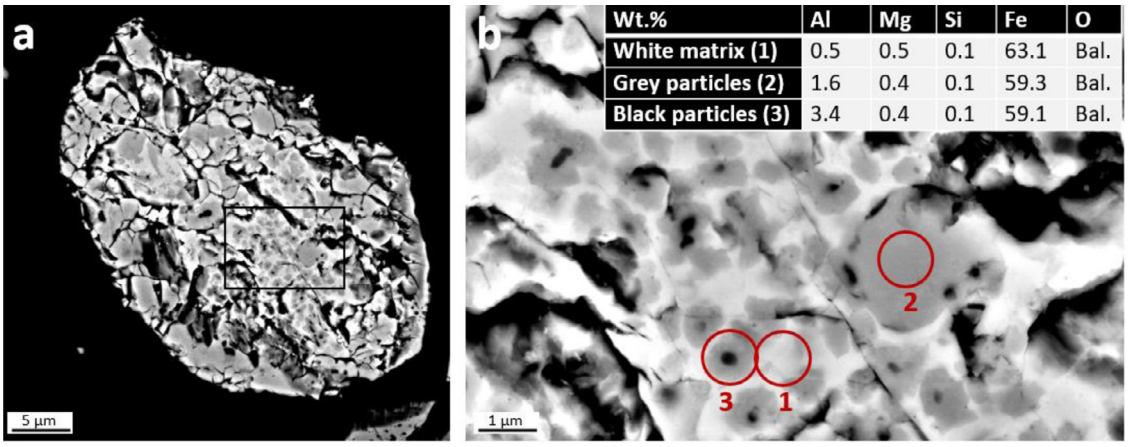

Wt.%	Al	Mg	Si	Fe	O
White matrix (1)	0.5	0.5	0.1	63.1	Bal.
Grey particles (2)	1.6	0.4	0.1	59.3	Bal.
Black particles (3)	3.4	0.4	0.1	59.1	Bal.

Fig. 8. (a) Overview and (b) magnified SEM image of an OxPro combusted particle containing Mg, Al and Si impurities quantified by SEM EDS.

the OxAir powder (Fig. 9(b)). It is unlikely that two different mechanisms are activated in OxPro and OxAir powders, resulting in two different "Matryoshka doll" arrangements. Therefore, these peculiar microstructures probably do not result from the combustion mechanism itself but from a post-combustion handling of the powders, with smaller particles entering the larger particles opened by micro-explosion or crack propagation during/after the combustion process.

The spherical ignited particles appear to have melted during the combustion process, as attested by their spherical shape as well as the dendritic morphology on the surface of the particles (Fig. 5 and 9). The flame temperature (up to 1900–2200 °C) largely surpasses the melting temperature of iron (1538 °C) and its oxides (1596 °C), and is close to the adiabatic flame temperature [14,22], indicative of a diffusion-controlled combustion mode [16,41]. A dendritic morphology is also observed in the large cavities in the center of the particles (Fig. 6(a)), showing that the inner porosities were formed during the solidification process. A process similar to the formation of shrinkage cavities during metal casting could explain these inner voids. The volume of the initial iron particle strongly increases during the combustion process due to its melting at high temperature and to the oxygen intake [12,14]. Considering the solidification starting at the external surface of the droplet towards its interior, i.e. keeping the same external diameter, the relative diameter of the internal void can be estimated from the density of the liquid and from the density of the solid iron oxide. Considering solidification into magnetite, with a density of 4.73 g.cm^{-3} at 1400 °C estimated using FactSage [42], and a density of the iron oxide liquid, reported to vary in the range of 3.6–4.9 g.cm^{-3} at 2500 °C by Steinberg et al. [43], a maximum size of the inner void of 60% of the particle diameter is expected from the solidification process alone. Based on image analysis of the SEM images, 90% of the OxPro particles as well as 84% of the ignited OxAir particles present a porosity diameter below 60% of the particle diameter. However, some very thin shells have also been observed, with an inner void diameter up to 80% of the particle diameter. For the latter, the solidification process cannot solely explain the large internal porosity observed.

In addition to the large internal porosity, exploded particles are observed. Micro-explosions have been reported by several authors during the combustion of iron powders [8,9,15,41], generally shortly after the maximum temperature, when the gradient of temperature between the particle and the surrounding environment is at a maximum [41]. It results from a relative increase of the internal pressure inside the particles compared to the surrounding pressure, which is believed to originate from the expansion of a gas present inside the powders [9,11–13,41]. The accumulation and entrapment of gas inside the liquid droplets could also explain the larger inner porosity diameter sometimes observed, when the pressure gradient is not large enough to explode the particle. Three sources of gas entrapment can be considered: (i) gaseous product of a chemical reaction, (ii) evaporation of iron, (iii) diffusion and dissolution of the surrounding gas as oxygen. The occurrence of these different sources has been approached using thermodynamic calculations, considering an adiabatic oxidation of the initial iron powder in air. The same simulation was also applied with the addition of propane, and yielded the same qualitative results. It should be noted that a more complex simulation considering the kinetics of the reaction should be used to accurately represent the combustion process [44], but a thermodynamic simulation using adiabatic conditions constitutes a good first approximation for a combustion process in the diffusion-controlled mode [16]. Fig. 10(a) presents the temperature evolution simulated by Thermocalc [37], with a maximum adiabatic flame temperature of 2000 °C, corresponding well to the spectrometer measurements (Supplementary Figure S1). Fig. 10(b) presents the variation of the partial pressure of the different gas species, as a function of the total oxygen amount added to the open system and the calculated adiabatic temperature, as explained in Section 2. A detailed evolution of the stabilized phases as well as a magnification of Fig. 10(b) for smaller values of partial pressures are given in Supplementary Figure S4. The production of carbon mono/di-oxide gas is favored at the very beginning of the combustion process, which means that the oxidation of the carbon present inside the initial powders is expected to occur as soon as the diffusion of the species allows their reaction. The production of gaseous sulfur di-oxide is also predicted at the maximum temperature (Supplementary Figure S5) at a smaller extent (20% less moles of sulfur predicted in the gaseous phase compared with carbon). In accordance with this hypothesis, a decrease in the carbon and sulfur content of the particle is indeed observed in the combusted particles. The first source of internal porosity could therefore be the oxidation of the carbon/sulfur present in the initial iron powder.

At the maximum temperature, an increase in the partial pressure of pure iron is also predicted. The occurrence of evaporation/dissociation of metal (oxide) during the combustion of iron powder has been proven by the observation of a vapor phase halo surrounding the particles using high-speed imaging [9,11,12,41]. Moreover, iron oxide nanoparticles were regularly observed in the combusted products [6,8,9,11]. While nanoparticles production has been mostly reported for excess oxygen conditions (more than 21

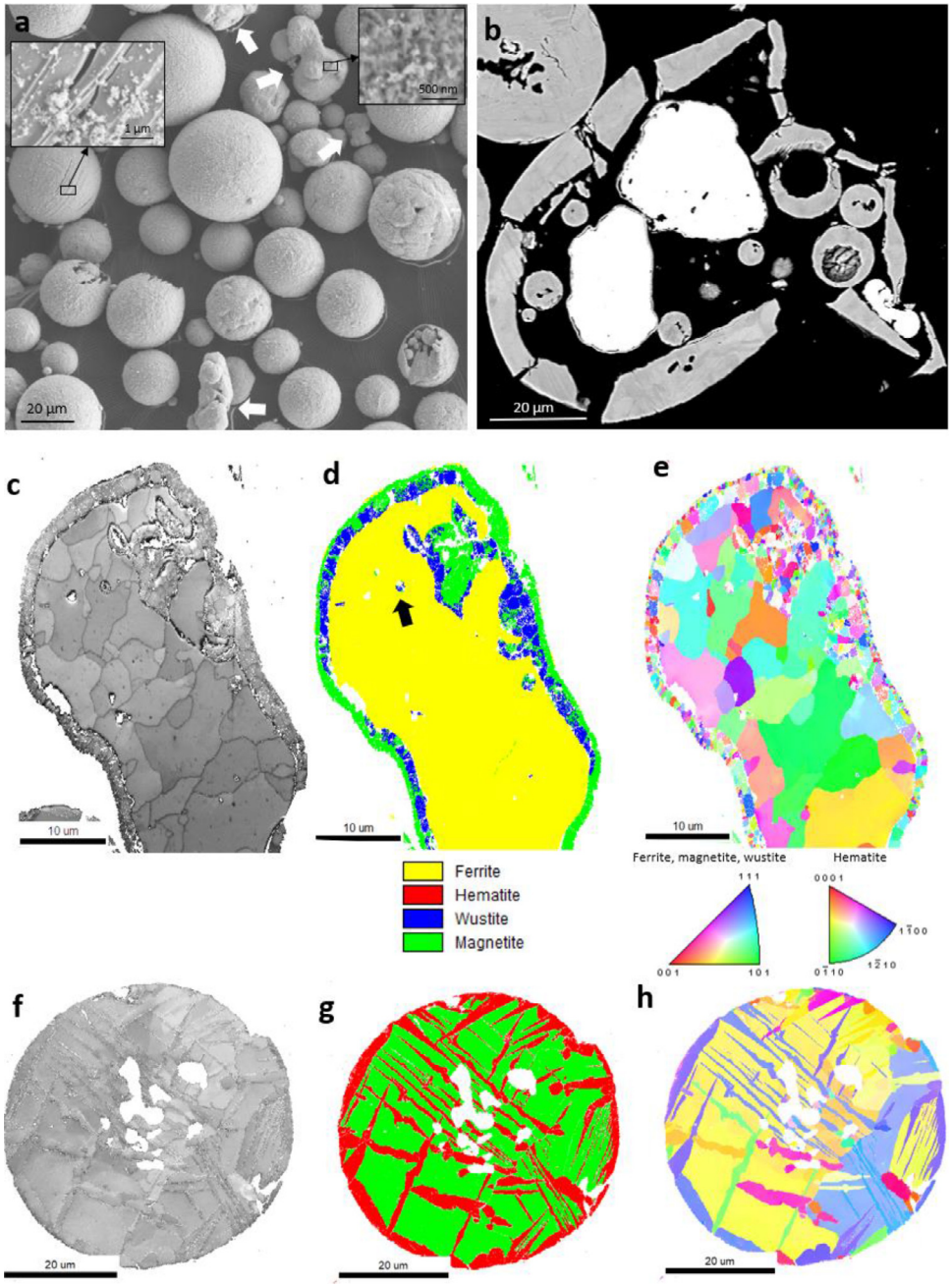

Fig. 9. Analysis of OxAir powder. (a) SEM image of their morphology, with magnified images of the surface of spherical and irregular-shape particles, the latter highlighted by white arrows. (b) SEM image of the cross-section of an exploded particle, containing both spherical and irregular-shaped particles inside. (c), (f) EBSD image quality map, (d), (g) phase map and (e), (h) crystalline orientation map of (c-e) an irregular-shape particle and (f-h) a spherical particle.

at.% oxygen) [6,9,11,17,41], some nanoparticles have also been observed for normal atmospheric conditions (21 at.% oxygen) [8,9,12]. As presented in Figs. 5(d) and 9(a), nanoparticles are also observed on the surface of the combusted products. Moreover, nanoparticles were also observed on the internal walls throughout the combustion system and in the filters. Their reddish color indicates that they are probably constituted of hematite [13]. According to the Thermocalc simulation (Fig. 10(b) and Supplementary Figure S4), the evaporation of iron is favored compared with the formation of iron oxide vapor and to the other metallic impurities present, which agrees well with the study of Ning et al. [9]. The increase in partial pressure of copper around the maximum temperature indicates a possible copper evaporation together with iron, although no decrease in copper content was measured in the combusted particles (Table 1). A second source of gas could therefore come from the evaporation of pure iron.

When considering an adiabatic process as simulated in Fig. 10, the maximum temperature is reached for an oxygen content corresponding to the solubility limit of the iron oxide liquid. For higher oxygen content, at the beginning of the cooling process, gaseous oxygen bubbles will form inside the liquid droplets, which is illustrated by the increase in the partial pressure of oxygen for an oxygen content above 32 g in Fig. 10(b). A third source of gas encapsulation is therefore the formation of oxygen-rich gas bubbles that will arise for sufficiently large oxygen concentrations. Similarly, gas encapsulation could come from the diffusion and dissolution of other species from the surrounding gas (nitrogen, water vapor) inside the liquid droplets [41].

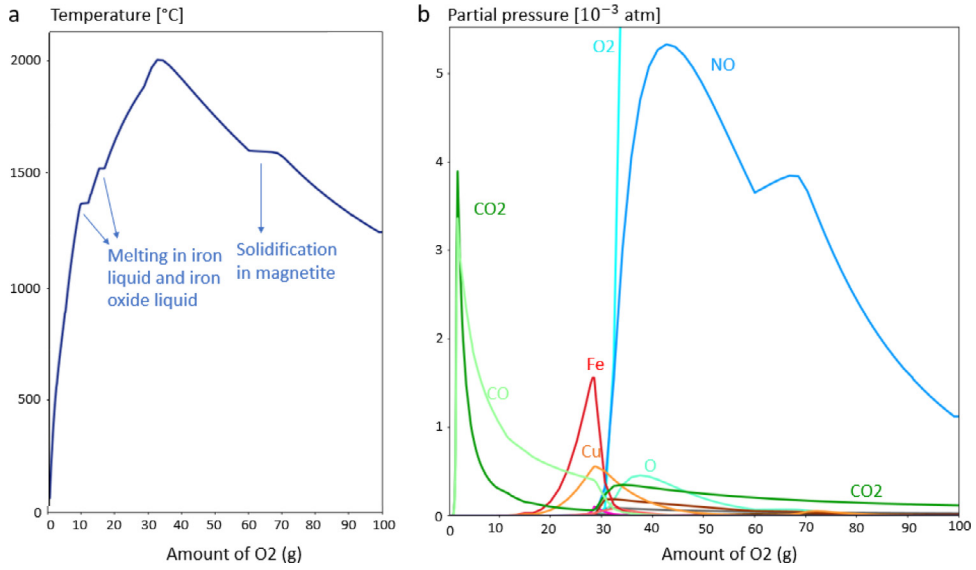

Fig. 10. Thermodynamic simulation (Thermocalc) of the combustion of 100 g of the initial iron powder (Table 1) for equilibrium adiabatic conditions. (a) Flame temperature, (b) Partial pressure of the different species in the gas phase as a function of the added amount of oxygen to the system (for each gram of oxygen added, the relative amount of nitrogen is also added to keep a ratio of 79 at.% N2 + 21 at.% O2).

The thermodynamic simulation predicts magnetite formation during solidification (Fig. 10(a)), which agrees with the temperature of the solidification plateau measured between 1480 °C and 1610 °C during single laser ignited iron combustion [9], close to the temperature range between 1424 °C and 1596 °C for magnetite solidification. While the large heating and cooling rate involved in the combustion of iron particles do not respect the equilibrium conditions, the Fe-O binary phase diagram can still be used as a guide to predict the expected phase transformations during cooling of iron oxide droplets. The exact concentration of oxygen of the liquid droplet when reaching the liquidus temperature is unknown, but hypotheses can be taken. Based on a diffusion model, Ning et al. [8] estimated a concentration around 46 at.% O inside 30 µm-particle at the maximum temperature. Moreover, they noticed a linear cooling rate indicating that oxidation continues during cooling of the particle. A concentration of oxygen larger than 46 at.% is therefore expected at the beginning of the solidification. The minimum oxygen concentration in the iron oxide droplets during solidification can be estimated from the least oxidized particle observed in the OxPro powder, presented in Fig. 7: the particle contains wüstite in an interdendritic region in the center of the particle. The formation of wüstite in-between dendrites of magnetite can be expected for a concentration of oxygen between 54.2 at.% and 57 at.% (Fig. 11). The area fraction of interdendritic microstructure of 10% was estimated using ImageJ in the central region of the particle presented in Fig. 7, corresponding to an oxygen concentration around 56.8 at.%. Fig. 11(a) presents the expected microstructural evolution for a solidification starting around 56.8 at.% O. Solidification starts around 1580 °C by the growth of magnetite dendrites in liquid iron oxide, forming an inner void by solidification shrinkage and/or gas accumulation inside the particle, as discussed previously. At 1424 °C, a peritectic transformation takes place, forming wüstite at the interface between the remaining iron oxide liquid and the magnetite dendrites. During further cooling, dendrites of magnetite are expected to grow at the expense of the interdendritic wüstite formed as the solubility of oxygen in wüstite decreases with temperature. Instead, small magnetite islands are observed inside the wüstite matrix in Fig. 7. It can be expected that the magnetite islands originate from an oversaturation of oxygen inside wüstite, resulting from the large cooling rate (estimated around 85,000 K/s after the solidification plateau for single laser ignited iron particles [9]). After solidification, the oxidation of magnetite to hematite continues at the surface of the particle. According to Zheng et al. [45,46], oxidation of magnetite to hematite is mainly dominated by the solid-state diffusion of iron cations from the magnetite matrix to the surface of the particle. Hematite grains first nucleate and grow at the surface of the particle, forming a dense and continuous shell. The outward diffusion of iron cations causes the formation of plate-like features at the surface of the particles [45,46], such as the ones observed in Fig. 5(a)-(b). Then, hematite plates grow from the surface to the center of the particle, as presented in Fig. 6, 7, 9(f)-(h). According to Zheng et al. [45,46], this morphology originates from a favored diffusion of iron cations along preferred crystalline orientations in the magnetite matrix [45,46].

The absence of wüstite in the other combusted particles can be explained by a larger oxidation rate, either before or after solidification. Fig. 11(b) presents the schematic microstructural evolution for an oxygen concentration between 57.14 at.% and 57.67 at.% upon solidification. The formation of wüstite is hindered and only magnetite solidifies from the liquid state. Hematite plates then nucleate and grow from the external surface of the particle. Fig. 11(c) presents the schematic microstructural evolution expected for a concentration of oxygen above 57.67 at.%. Bubbles of oxygen gas are expected to form first in the liquid iron oxide, then inside the solid matrix of magnetite. As discussed previously, these oxygen bubbles could participate in the formation of inner porosities as well as micro-explosion events. However, hematite would form at the interface between the magnetite matrix and the oxygen bubbles during the solidification of the particle. Yet, hematite plates were mostly observed growing from the external surface of most particles (Figs. 7(f) and 9(g)). Hematite plates were only observed growing from the largest inner voids, as in Fig. 7(b), showing that the formation of inner oxygen-rich bubble gas would result in a significant expansion of the liquid droplet. Yet, these voids could have been opened to the external environment by micro-explosions before the hematite growth. A more detailed 3D analysis would be required in that case to identify if hematite can nucleate and grow from closed porosity, demonstrating in that case the presence of oxygen bubbles. For most particles presenting only hematite plates at the external surface, one can state that the oxygen concentration of the

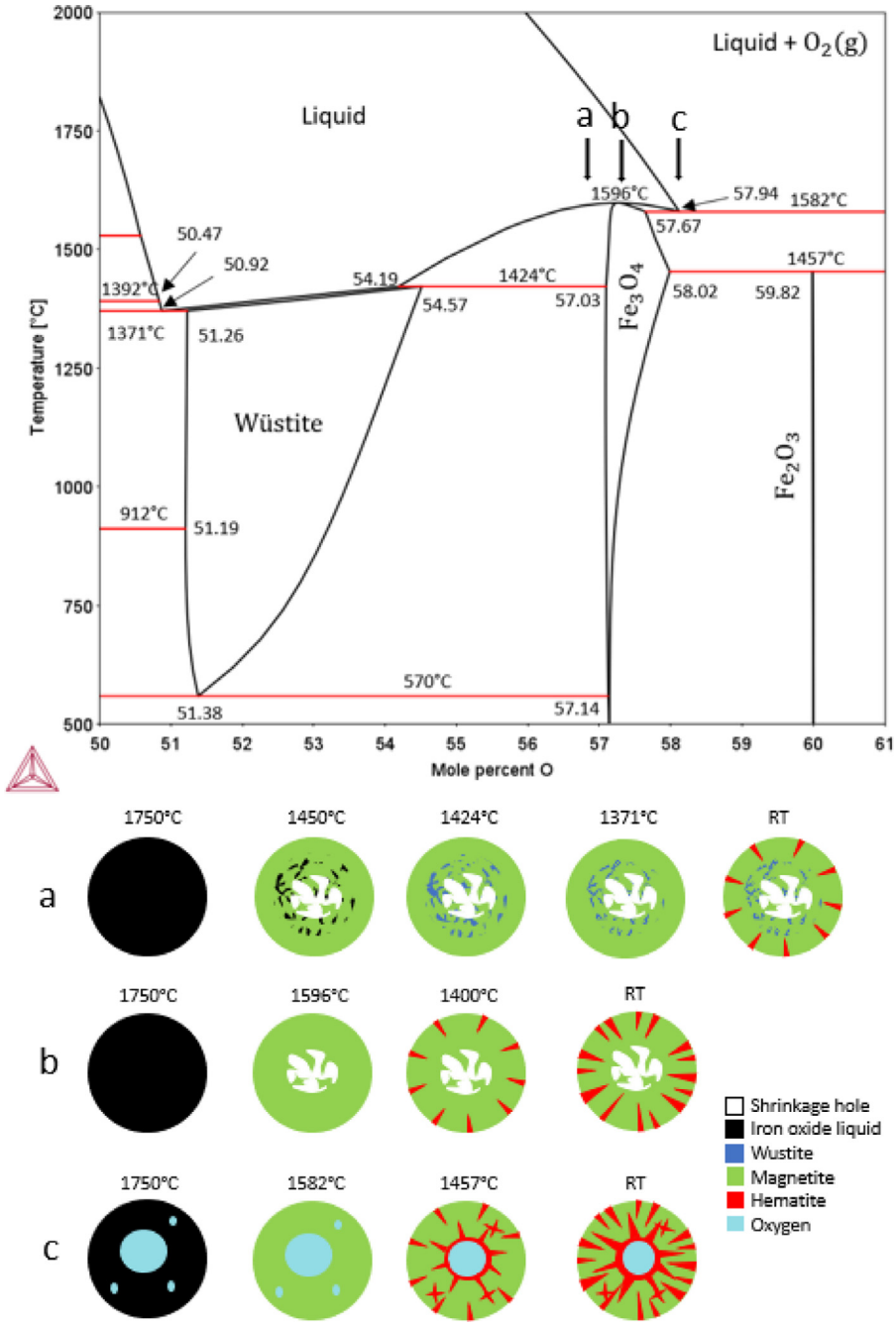

Fig. 11. Phase diagram of the binary Fe – O system for the oxygen concentration between 50 and 61 at.%, drawn with the aid of the Thermocalc software. (a-c) Schematic representation of the phase transformations and microstructural evolution during cooling of ignited iron particles for increasing oxygen concentrations at the beginning of the solidification.

liquid iron oxide was comprised between 56.8 at.% and 57.67 at.% O.

The full combustion potential of these powders was not reached as the initial pure iron powder did not completely oxidize into hematite. The oxidation rate from magnetite to hematite was indeed reported to strongly decrease after the formation of a continuous hematite shell around the particle, limiting ionic diffusion through the dense hematite layer [45]. However, the oxidation from magnetite to hematite represents only a small fraction of the heat release during the combustion. Based on their enthalpy of formation at 25 °C, the oxidation from ferrite to magnetite releases 6675 kJ/kg, compared with 7379 kJ/kg for the oxidation from ferrite to hematite. 95% of the heat potential of the iron powders was therefore released during their ignition, based on the XRD measurements (Fig. 4). Moreover, Zheng et al. [34] reported that a larger reduction degree was obtained during the hydrogen-based reduction of powders composed of both hematite and magnetite phases by promoting both the diffusion and the chemical reaction during the end of the reduction process, compared with the reduction of pure hematite powders. The formation of multiple hematite grains particularly favors hydrogen-based reduction at relatively high temperatures (750 °C-825 °C) [47], generally limited by solid-state diffusion through the iron layer at the end of the reduction process [34,35,48]. After the reduction of an initially pure magnetite particle, a single dense block of wüstite surrounded by a thick iron layer is obtained, while for hematite-magnetite particles, numerous porous wüstite islands are observed, each surrounded by a thinner iron shell. Wolfinger *et al.* [47] explained that the

increased reduction degree obtained by the presence of hematite plates is due to the creation of multiple crystalline defects during the growth of the hematite grains, that will act as favorable nucleation sites during the reduction. These defects will also promote the solid-state diffusion of iron atoms. Finally, the presence of hematite is also interesting for the fluidized bed hydrogen-based reduction of the powder, as it increases the defluidisation time compared with the reduction of pure magnetite powders and hence increase the final reduction degree [34].

The porosity and crack network formed inside the combusted iron particles have also a major impact on the efficiency of the iron powder fuel. The presence of a large porosity level can lead to the embrittlement and fragmentation of the powder which would be detrimental for the cyclic use of the powder. Moreover, increased porosity levels will lead to decreased volume energy density of the powder fuel. However, the presence of porosity might have a positive influence on the subsequent reduction efficiency. No significant beneficial effect of the presence of close porosity was observed during the hydrogen-based solid-state reduction of iron oxide [35]. However, it can be expected that open porosities, i.e. when the inner cavities are linked to the external surface, will strongly accelerate the reduction kinetics through an easy access of hydrogen and of the reduction products to the center of the particles. Using image analysis on SEM images, a close porosity level of 4.7% was estimated for OxAir powder, and of 6.1% for OxPro powder (and of 6.0% for OxAir powder when removing the iron particles from the analysis). However, this porosity level is overestimated as the analysis was applied in 2D, while the porosities considered as closed in 2D might be open to the external surface considering the 3D morphology of the particle. A more precise close porosity level was evaluated using pycnometer and XRD measurements, based on the theoretical densities of the different phases at room temperature. A close porosity level of 0.6% was obtained in the initial powder, increasing to 1.7% in the OxPro powder. The close porosity level in the OxAir particles is more difficult to assess because of the larger standard deviation of the phase distribution (Fig. 4), depending on the concentration of non-ignited Fe particles. The close porosity level estimated in the OxAir particles ranges from 0.3 to 2.2%. Such low levels of close porosities compared with the large inner cavities formed inside the combusted products can be explained by the cracks formed between the inner porosity and the external surface. The shape of the hematite lenticular plates and their crystalline orientation remains unchanged even when completely separated by several cracks (Figs. 7(a-c)), indicating that the nucleation and propagation of these cracks occurred after the nucleation and growth of the hematite grains, i.e. at the end of the combustion process. These cracks could result from large internal stresses at the interface of the phase boundaries, created during the fast solidification and cooling. However, many cracks are not linked to the phase boundaries, and are observed to propagate through the hematite plates, or propagate from the external surface or from an internal void (Figs. 5, 6 and 7). Cracking can also be expected due to the multiple collisions between the particles and with the combustor walls/cyclone. Effects of sample handling and metallographic preparation can also not be ruled out.

More investigations are needed to better understand the cracks and porosity evolution inside the combusted particles, as it will play an essential role during the subsequent reduction process by facilitating the diffusion of gaseous reactants and products. The origin and mechanisms of micro-explosions, crack nucleation and propagation during the combustion of iron particles also deserves more investigations. Elucidating the mechanisms of the combustion of the iron particles will allow a better control of its microstructure and morphology evolution, essential to improve the efficiency of the reduction process, hence of the complete life cycle of iron-based metallic fuel.

5. Conclusions

In this study, the microstructure and morphology evolution of pure iron powder was investigated during its combustion using either only pre-heated air or using a propane pilot flame. A higher oxidation level was observed when using propane due to a facilitated ignition of the powders.

- The combusted powders are mostly constituted of hollow spheres, with a magnetite matrix and hematite lenticular plates. Significant internal porosity is formed during solidification, probably due to the solidification process and to gas encapsulation. The hypothesis of gas encapsulation inside the liquid droplets is further supported by the observation of multiple exploded particles. Moreover, the observation of nanoparticles on the combusted product favors the hypothesis of metal evaporation during the combustion process.
- The different phase transformations occurring during the combustion of ignited particles were identified, including a transformation to the liquid state at the larger temperatures (2000–2200 °C). The solidification path was explained by the nucleation and growth of magnetite dendrites from the liquid state, and the nucleation and growth of hematite grains in the solid state. The obtained microstructure indicates that the oxygen concentration of most of the non-exploded analyzed particles was comprised between 56.8 and 57.7 at.% O at the beginning of the solidification process.
- A relatively low close porosity level is measured by pycnometer in the combusted particles (between 1 and 2%), considering the large porosity observed in the cross-sections. The inner porosities are expected to be linked to the external surface of the particle through micro explosion and crack nucleation and growth. Cracking mainly occurs at the end of the combustion process, after the nucleation and growth of hematite laths.

Further studies will focus on the porosity and cracks network and phase distribution inside the combusted particles. Both will majorly influence the final morphology and open porosity level of the particles, which are essential to control for the subsequent reduction process.

Declaration of Competing Interest

The authors declare that they have no known competing financial interests or personal relationships that could have appeared to influence the work reported in this paper.

Acknowledgments

We thank Christian Bross, Monika Nellessen and Katja Angenendt for their support to the metallography lab and SEM facilities at MPIE, Benjamin Breitbach for the support to the X-ray diffraction facilities, Herbert Faul for the pycnometer measurement and Daniel Kurz for the chemical analysis of the powders at MPIE. We gratefully acknowledge the support of Pometon S.p.A. LC acknowledges the financial support through the postdoctoral scholarship program of the Max-Planck Society. IRSF acknowledges financial support through CAPES (Coordenação de Aperfeiçoamento de Pessoal de NívelSuperior) & Alexander von Humboldt Foundation (grant number 88881.512949/2020–01). YM acknowledges financial support through Walter Benjamin Programme of the Deutsche Forschungsgemeinschaft (project number 468209039). H.S. acknowledges funding through the Heisenbergprogramm of the Deutsche Forschungsgemeinschaft (grant SP1666/2). TU/e gratefully acknowledges the support of Shell, the European Research Council (grant agreement no. 884916), the Eu-

ropean Regional Development Fund and Provincie Noord-Brabant within the OPZUID program.

Supplementary materials

Supplementary material associated with this article can be found, in the online version, at doi:10.1016/j.actamat.2022.118261.

References

[1] G. Thomas, in: Proceedings of the 2000U.S. DOE Hydrogen Program Review, National Renewable Energy Laboratory, San Ramon, 2000 U.S. Department of Energy (Ed.).

[2] J.M. Bergthorson, Recyclable metal fuels for clean and compact zero-carbon power, Prog. Energy Combust. Sci. 68 (2018) 169–196, doi:10.1016/j.pecs.2018.05.001.

[3] D. Mignard, C. Pritchard, A review of the sponge iron process for the storage and transmission of remotely generated marine energy, Int. J. Hydrogen Energy 32 (2007) 5039–5049, doi:10.1016/j.ijhydene.2007.06.032.

[4] J.M. Bergthorson, S. Goroshin, M.J. Soo, P. Julien, J. Palecka, D.L. Frost, D.J. Jarvis, Direct combustion of recyclable metal fuels for zero-carbon heat and power, Appl. Energy 160 (2015) 368–382, doi:10.1016/j.apenergy.2015.09.037.

[5] P. Julien, J.M. Bergthorson, Enabling the metal fuel economy: green recycling of metal fuels, Sustainable Energy Fuels 1 (2017) 615–625, doi:10.1039/c7se00004a.

[6] H. Wiinikka, T. Vikström, J. Wennebro, P. Toth, A. Sepman, Pulverized Sponge Iron, a Zero-Carbon and Clean Substitute for Fossil Coal in Energy Applications, Energy Fuels 32 (2018) 9982–9989, doi:10.1021/acs.energyfuels.8b02270.

[7] L. Dirven, N.G. Deen, M. Golombok, Dense energy carrier assessment of four combustible metal powders, Sustainable Energy Technol. Assess. 30 (2018) 52–58, doi:10.1016/j.seta.2018.09.003.

[8] D. Ning, Y. Shoshin, J.A. van Oijen, G. Finotello, L.P.H. de Goey, Burn time and combustion regime of laser-ignited single iron particle, Combust. Flame 230 (2021) 111424, doi:10.1016/j.combustflame.2021.111424.

[9] D. Ning, Y. Shoshin, M. van Stiphout, J. van Oijen, G. Finotello, L.P.H. de Goey, Temperature and phase transitions of laser-ignited single iron particle, Combust. Flame 236 (2022) 111801, doi:10.1016/j.combustflame.2021.111801.

[10] J. Huang, S. Li, D. Sanned, L. Xu, S. Xu, Q. Wang, M. Stiti, Y. Qian, W. Cai, E. Berrocal, M. Richter, M. Aldén, Z. Li, A detailed study on the microexplosion of burning iron particles in hot oxidizing environments, Combust. Flame (2021), doi:10.1016/j.combustflame.2021.111755.

[11] S. Li, D. Sanned, J. Huang, E. Berrocal, W. Cai, M. Aldén, M. Richter, Z. Li, Stereoscopic high-speed imaging of iron microexplosions and nanoparticle-release, Opt. Express 29 (2021) 34465, doi:10.1364/oe.434836.

[12] P. Tóth, Y. Ögren, A. Sepman, P. Gren, H. Wiinikka, Combustion behavior of pulverized sponge iron as a recyclable electrofuel, Powder Technol. 373 (2020) 210–219, doi:10.1016/j.powtec.2020.05.078.

[13] N.I. Poletaev, M.Y. Khlebnikova, Combustion of Iron Particles Suspension in Laminar Premixed and Diffusion Flames, Combust. Sci. Technol. (2020) 1–22, doi:10.1080/00102202.2020.1812588.

[14] J. Huang, S. Li, W. Cai, Y. Qian, E. Berrocal, M. Aldén, Z. Li, Quantification of the size, 3D location and velocity of burning iron particles in premixed methane flames using high-speed digital in-line holography, Combust. Flame 230 (2021) 111430, doi:10.1016/j.combustflame.2021.111430.

[15] P. Julien, S. Whiteley, S. Goroshin, M.J. Soo, D.L. Frost, J.M. Bergthorson, Flame structure and particle-combustion regimes in premixed methane-iron-air suspensions, Proc. Combust. Inst. 35 (2015) 2431–2438, doi:10.1016/j.proci.2014.05.003.

[16] M. McRae, P. Julien, S. Salvo, S. Goroshin, D.L. Frost, J.M. Bergthorson, Stabilized, flat iron flames on a hot counterflow burner, Proc. Combust. Inst. 37 (2019) 3185–3191, doi:10.1016/j.proci.2018.06.134.

[17] J. Palečka, J. Sniatowsky, S. Goroshin, A.J. Higgins, J.M. Bergthorson, A new kind of flame: observation of the discrete flame propagation regime in iron particle suspensions in microgravity, Combust. Flame 209 (2019) 180–186, doi:10.1016/j.combustflame.2019.07.023.

[18] J. Palečka, S. Goroshin, A.J. Higgins, Y. Shoshin, P. de Goey, J.-.R. Angilella, H. Oltmann, A. Stein, B. Schmitz, A. Verga, S. Vincent-Bonnieu, W. Sillekens, J.M. Bergthorson, Percolating Reaction–Diffusion Waves (PERWAVES)—Sounding rocket combustion experiments, Acta Astronaut. 177 (2020) 639–651, doi:10.1016/j.actaastro.2020.07.033.

[19] M. Soo, X. Mi, S. Goroshin, A.J. Higgins, J.M. Bergthorson, Combustion of particles, agglomerates, and suspensions – A basic thermophysical analysis, Combust. Flame 192 (2018) 384–400, doi:10.1016/j.combustflame.2018.01.032.

[20] T. Hazenberg, J.A. van Oijen, Structures and burning velocities of flames in iron aerosols, in: Proceedings of the Combustion Institute, Elsevier Ltd, 2021, pp. 4383–4390, doi:10.1016/j.proci.2020.07.058.

[21] E.I. Senyurt, E.L. Dreizin, At what ambient temperature can thermal runaway of a burning metal particle occur? Combust. Flame 236 (2022), doi:10.1016/j.combustflame.2021.111800.

[22] F.D. Tang, S. Goroshin, A.J. Higgins, Modes of particle combustion in iron dust flames, Proc. Combust. Inst. 33 (2011) 1975–1982, doi:10.1016/j.proci.2010.06.088.

[23] X.C. Mi, A. Fujinawa, J.M. Bergthorson, A quantitative analysis of the ignition characteristics of fine iron particles, Combust. Flame (2022) 240, doi:10.1016/j.combustflame.2022.112011.

[24] J. Païdassi, Sur la cinétique de l'oxydation du fer dans l'air dans l'intervalle 700-1250 °C, Acta Metall. 6 (1958) 184–194.

[25] A.V. Roshchin, V.E. Roshchin, Diffusion of Anions and Cations in Oxide Crystal Lattices during the Reduction and Oxidation of Metals, Russ. Metall. (2003) 1–5.

[26] F. Li, Z. Sun, S. Luo, L.S. Fan, Ionic diffusion in the oxidation of iron - Effect of support and its implications to chemical looping applications, Energy Environ. Sci. 4 (2011) 876–880, doi:10.1039/c0ee00589d.

[27] T. Hirano, K. Sato, Y. Sato, J. Sato, Prediction of metal fire spread in high pressure oxygen, Combust. Sci. Technol. 32 (1983) 137–159, doi:10.1080/00102208308923656.

[28] T. Hirano, J. Sato, Fire spread along structural metal pieces in oxygen, J. Loss Prev. Process Ind. 6 (1993) 151–157.

[29] M. Muller, H. El-Rabii, R. Fabbro, Liquid phase combustion of iron in an oxygen atmosphere, J. Mater. Sci. 50 (2015) 3337–3350, doi:10.1007/s10853-015-8872-9.

[30] J.H. Sun, R. Dobashi, T. Hirano, Combustion Behavior of Iron Particles Suspended in Air, Combust. Sci. Technol. 150 (2000) 99–114, doi:10.1080/00102200008952119.

[31] D. Spreitzer, J. Schenk, Reduction of iron oxides with hydrogen—a review, Steel Res. Int. 90 (2019) 1900108, doi:10.1002/srin.201900108.

[32] A. Pineau, N. Kanari, I. Gaballah, Kinetics of reduction of iron oxides by H2. Part II: low temperature reduction of magnetite, Thermochim. Acta 456 (2007) 75–88, doi:10.1016/j.tca.2005.10.004.

[33] A. Zare Ghadi, M.S. Valipour, S.M. Vahedi, H.Y. Sohn, A Review on the Modeling of Gaseous Reduction of Iron Oxide Pellets, Steel Res. Int. 91 (2020) 1900270, doi:10.1002/srin.201900270.

[34] H. Zheng, D. Spreitzer, T. Wolfinger, J. Schenk, R. Xu, Effect of Prior Oxidation on the Reduction Behavior of Magnetite-Based Iron Ore During Hydrogen-Induced Fluidized Bed Reduction, Metall. Mater. Trans. B 52 (2021) 1955–1971, doi:10.1007/s11663-021-02215-5.

[35] S.H. Kim, X. Zhang, Y. Ma, I.R. Souza Filho, K. Schweinar, K. Angenendt, D. Vogel, L.T. Stephenson, A.A. El-Zoka, J.R. Mianroodi, M. Rohwerder, B. Gault, D. Raabe, Influence of microstructure and atomic-scale chemistry on the direct reduction of iron ore with hydrogen at 700°C, Acta Mater. 212 (2021) 116933, doi:10.1016/j.actamat.2021.116933.

[36] J. Schindelin, I. Arganda-Carreras, E. Frise, V. Kaynig, M. Longair, T. Pietzsch, S. Preibisch, C. Rueden, S. Saalfeld, B. Schmid, J.-.Y. Tinevez, D.J. White, V. Hartenstein, K. Eliceiri, P. Tomancak, A. Cardona, Fiji: an open-source platform for biological-image analysis, Nat. Methods 9 (2012) 676–682, doi:10.1038/nmeth.2019.

[37] J.O. Andersson, T. Helander, L. Höglund, P.F. Shi, B. Sundman, Thermo-Calc and DICTRA, Computational tools for materials science, Calphad 26 (2002) 273–312.

[38] M. Hillert, Phase Equilibria, Phase Diagrams and Phase Transformations: Their Thermodynamic Basis, Cambridge University Press, 2007.

[39] R.M. Cornell, U. Schwertmann, The Iron Oxides, John Wiley, 2003.

[40] R.Y. Chen, W.Y.D. Yuen, A Study of the Scale Structure of Hot-Rolled Steel Strip by Simulated Coiling and Cooling, Oxid. Met. 53 (2000) 539–560.

[41] J. Huang, S. Li, D. Sanned, L. Xu, S. Xu, Q. Wang, M. Stiti, Y. Qian, W. Cai, E. Berrocal, M. Richter, M. Aldén, Z. Li, A detailed study on the microexplosion of burning iron particles in hot oxidizing environments, Combust. Flame (2021) 111755, doi:10.1016/j.combustflame.2021.111755.

[42] C.W. Bale, E. Bélisle, P. Chartrand, S.A. Decterov, G. Eriksson, A.E. Gheribi, K. Hack, I.H. Jung, Y.B. Kang, J. Melançon, A.D. Pelton, S. Petersen, C. Robelin, J. Sangster, P. Spencer, M.-.A. van Ende, FactSage Thermochemical Software and Databases, Calphad 54 (2016) 35–53.

[43] T.A. Steinberg, J. Kurtz, D.B. Wilson, The Solubility of Oxygen in Liquid Iron Oxide During the Combustion of Iron Rods in High-Pressure Oxygen, Combust. Flame 113 (1998) 27–37.

[44] E.I. Senyurt, E.L. Dreizin, At what ambient temperature can thermal runaway of a burning metal particle occur? Combust. Flame 236 (2022) 111800, doi:10.1016/j.combustflame.2021.111800.

[45] H. Zheng, J. Schenk, D. Spreitzer, T. Wolfinger, O. Daghagheleh, Review on the Oxidation Behaviors and Kinetics of Magnetite in Particle Scale, Steel Res. Int. 92 (2021) 2000687, doi:10.1002/srin.202000687.

[46] H. Zheng, J. Schenk, R. Xu, O. Daghagheleh, D. Spreitzer, T. Wolfinger, D. Yang, Y. Kapelyushin, Surface Morphology and Structural Evolution of Magnetite-Based Iron Ore Fines During the Oxidation, Metall. Mater. Trans. B (2022), doi:10.1007/s11663-022-02475-9.

[47] T. Wolfinger, D. Spreitzer, H. Zheng, J. Schenk, Influence of a Prior Oxidation on the Reduction Behavior of Magnetite Iron Ore Ultra-Fines Using Hydrogen, Metall. Mater. Trans. B 53 (2022) 14–28, doi:10.1007/s11663-021-02378-1.

[48] K. He, Z. Zheng, Z. Chen, H. Chen, W. Hao, Kinetics of hydrogen reduction of Brazilian hematite in a micro-fluidized bed, Int. J. Hydrogen Energy 46 (2021) 4592–4605, doi:10.1016/j.ijhydene.2020.10.263.

[49] J.M. Bergthorson, Y. Yavor, J. Palecka, W. Georges, M. Soo, J. Vickery, S. Goroshin, D.L. Frost, A.J. Higgins, Metal-water combustion for clean propulsion and power generation, Appl. Energy 186 (2017) 13–27, doi:10.1016/j.apenergy.2016.10.033.